



In-plane implanting carbon rings into carbon nitride to intrigue nonradical photodegradation

Yu Yao^a, Yantao Wang^a, Teng Lu^c, Jinqiang Zhang^{a,*}, Kunsheng Hu^a, Huayang Zhang^a, Tara Pukala^b, Yun Liu^c, Xiaoguang Duan^{a,*}, Shaobin Wang^a

^a School of Chemical Engineering, The University of Adelaide, Adelaide, SA 5005, Australia

^b School of Physics, Chemistry and Earth Sciences, The University of Adelaide, SA 5005, Australia

^c Research School of Chemistry, The Australian National University, Canberra, ACT 2601, Australia

ARTICLE INFO

Keywords:

Carbon nitride
In-plane heterojunction
Nonradical
Photodegradation
Energy transfer

ABSTRACT

Photocatalysis has emerged as a prevailing and clean technology for water purification. In this work, we developed a facile approach for fabricating in-plane carbon/carbon nitride heterojunctions (CN-PDs) that induced 100 % photodegradation of naproxen under visible light irradiation in a nonradical manner. Experimental and simulation results collectively revealed that the incorporated carbon rings in carbon nitride (CN) significantly accelerate the charge dynamics of excitons, leading to a higher concentration of hot carriers. In addition, a lower intersystem crossing energy barrier was observed for the unique nanostructure compared to pristine CN, enabling an efficient energy-transfer-mediated oxygen activation to selectively generate singlet oxygen. An optimized composition of carbon rings (CN-PDs_{0.1}) enhanced the photodegradation of naproxen compared to CN. This study established the structure-activity relationships in selective photooxidation. The findings will benefit advanced design of high-performance nonmetal photocatalysts for organic wastewater treatment.

1. Introduction

Pharmaceuticals and personal care products (PPCPs) have been ubiquitously detected in wastewater matrices, which potentially pose negative impacts on human health and the ecosystems if not properly treated [1,2]. Among these substances, naproxen, a pharmaceutical compound, enters aquatic ecosystems through various pathways such as pharmaceutical manufacturing discharges and household wastewater. Although originally intended for medical use, the presence of naproxen in drinking water also gives rise to worries about unintentional human exposure. Its presence can disrupt aquatic organisms, affecting physiology, growth, and reproductive capabilities. While concentrations of naproxen in water sources are typically low, prolonged exposure could potentially contribute to antibiotic resistance and unintended health consequences. Due to its persistence and ability to accumulate in the environment, the removal of naproxen from water sources is crucial for maintaining the health of ecosystems [2,3]. Therefore, it is essential to prioritize the elimination of naproxen from water sources in order to effectively address potential risks to public health and the integrity of

ecosystems [4,5].

Fenton/Fenton-like technologies have been utilized to eliminate NPX in wastewater [6,7], while their reliance on activation reagents and generation of additional pollutants limit their practical applications [8]. Photocatalysis, on the other hand, is a clean and sustainable technology widely used for environmental remediation [9]. In this process, photo-induced electrons (e^-) and holes (h^+) participate in surface redox reactions to generate reactive oxygen species (ROS) (e.g., $\bullet OH$, $O_2^{\bullet -}$ and O_3), which can degrade pollutants into harmless compounds [10,11]. Till now, most reported photodegradation processes are radical-based processes [12], and the efficiency is limited by the short lifetime of free radicals and their substantial quenching by water background substances.

Photocatalysts used for photodegradation typically consist of metal nanoparticles with plasmonic properties [13], organic [14] and inorganic semiconductors [15], and their composites [16]. However, metal-based catalysts suffer from the limitation of being expensive and the risk of secondary contamination in heterogeneous reactions [8]. Metal-free photocatalysts, such as carbon nitride (CN), are therefore

* Corresponding authors.

E-mail addresses: jinqiang.zhang@adelaide.edu.au (J. Zhang), xiaoguang.duan@adelaide.edu.au (X. Duan).

<https://doi.org/10.1016/j.apcatb.2023.123363>

Received 6 June 2023; Received in revised form 15 September 2023; Accepted 4 October 2023

Available online 5 October 2023

0926-3373/© 2023 The Author(s). Published by Elsevier B.V. This is an open access article under the CC BY license (<http://creativecommons.org/licenses/by/4.0/>).

appealing for solar light harvesting and environmental remediation [14, 17–19]. Despite decades of efforts, the efficiency of CN for solar energy harvesting and waste removal remains unsatisfactory due to its low light absorption, small specific surface area (SSA), and sluggish charge dynamics [20]. Hybridizing CN with other active components to establish interfacial electric fields can improve light response capability and accelerate charge dynamics [21,22], but the enhancement is limited at the boundary of the heterojunction. The bulk properties of the parent photo-active compounds remain unchanged.

Fabrication of lateral heterostructure offers an intriguing approach for maximizing charge dynamics in carbon nitride-based composites through in-plane molecular engineering. For example, Che et al. incorporated aromatic carbon rings into the carbon nitride host using glucose as a carbon source, which significantly accelerated the separation rate of charge carriers and prolonged their lifetime for enhanced photocatalysis [23]. Carbon dots have also been used to fabricate carbon ring/carbon nitride in-plane heterojunction [24,25]. Although significant improvements in photocatalysis have been achieved with the unique structure, the percentage of carbocycles implantation remains low. Polymer dots (PDs) are emerging organic nanomaterials that possess a larger π -conjugated structure than small organic molecules but are less stable than carbon dots [26]. Therefore, PDs are good candidates as the source of carbon rings for constructing carbon/carbon nitride lateral heterojunctions.

In this work, PDs were synthesized and acted as the precursor of carbon rings for assembling carbon/carbon nitride in-plane heterojunctions. The abundant amino groups on the surface of PDs facilitated the adsorption of CN precursor molecules (i.e., urea) and promoted epitaxial growth of CN. The resulting planar heterojunction materials were used for the photodegradation of NPX, showing an intensified removal efficiency of organic pollutants through a nonradical mechanism. The structure-function relationship of the lateral heterostructure in photodegradation of NPX was then revealed through experimental and simulation results. Carbon rings will expedite the separation and transfer of photo-excited charge carriers in CN for direct injections into reactant molecules. Besides, the introduction of carbon rings into the carbon nitride matrix significantly reduced the energy barrier for intersystem crossing (ISC) from 0.31 eV in CN to 0.07 eV in CN-PDs_{0.1}. This reduction enabled enhanced energy-transfer-mediated oxygen activation, resulting in the production of more singlet oxygen, and thus a higher removal efficiency of organic pollutants via a non-radical mechanism. This work elucidates a non-radical photodegradation process in a unique lateral heterostructure. These findings will provide advance protocols for the design and manufacture of high-performance metal-free photocatalysts for efficient and eco-friendly treatment of water pollutants.

2. Methods and materials

2.1. Materials

Citric acid, urea, ammonium oxalate (AO), potassium dichromate (K₂Cr₂O₇), ethanol, ethylene diamine tetraacetic acid disodium salt dihydrate (EDTA-2Na), chloroform, 2,3,6-trimethylphenol (TMP), furfuryl alcohol (FFA), naproxen (NPX), sodium sulfate (Na₂SO₄), methanol, phenol, sulfamethoxazole (SMX), ibuprofen (IBP) (>98.0 %), bisphenol A (BPA), benzoic acid (BA), 4-chlorophenol (4-CP), acyclovir (ACV), acetaminophen (ACP), HPLC-grade acetonitrile and methanol were all purchased from Sigma-Aldrich. All the chemical reagents in this work were used without contamination. Ultra-pure water (18.2 M Ω -cm) was produced from a Milli-Q water purification system for all aqueous solutions. Tap water and river water were taken from Helen Mayo North building, The University of Adelaide, and the River Torrens, Adelaide, South Australia, respectively.

2.2. Synthesis of PDs

Polymer dots were prepared via a modified hydrothermal method. Briefly, 10 g of citric acid and 10 g of urea were dissolved in 75 mL pure water with continuous magnetic stirring for 30 min. The solution was then transferred to a 120 mL Teflon-sealed autoclave, which was heated up to 180 °C and maintained for 12 h. After natural cooling to room temperature, the obtained dark green suspension was centrifuged at 10,000 rpm for 20 min to remove the bulk particles. PDs were ultimately acquired after dialysis in 750 mL deionized water for 24 h and freeze-drying for 48 h.

2.3. Synthesis of in-plane carbon nitride/carbon heterojunction

Carbon rings were implanted into the carbon nitride matrix by a chemical epitaxial growth strategy. In a typical procedure, 20 g of urea and a certain amount (0.05, 0.1, 0.3 and 0.5 g) of PDs were dissolved into 50 mL pure water, followed by magnetic stirring for 30 min to form a transparent green solution. The water was then evaporated on a hot plate at 80 °C. The obtained solid sample was fully ground, and the resultant powder was subsequently calcined in a muffle furnace at 600 °C for 1.5 h at a ramping rate of 5 °C min⁻¹. The resultants were denoted as CN-PDs_x (x = 0.05, 0.1, 0.3 and 0.5). For comparison, CN was prepared with the same method in the absence of PDs.

2.4. Characterizations

X-ray powder diffraction (XRD) patterns were collected on a Rigaku MiniFlex 600 X-ray diffractometer. Transmission electron microscopy (TEM), high-resolution transmission electron microscopy (HRTEM), high-angle annular dark-field scanning transmission electron microscopy (HAADF-STEM) images and energy-dispersive X-ray spectroscopy (EDS) spectra were obtained on a FEI Titan Themis equipped with a JEOL 2100F microscope and a HAADF detector. A Nicolet 6700 Fourier transform infrared spectrometer was used to analyze functional groups on the prepared samples. X-ray photoelectron spectroscopy (XPS) (Thermo Scientific K-Alpha+) was applied to determine the surface compositions and chemical states of the obtained catalysts. The surface topography and surface potential measurements were conducted in air by a commercial Atomic force microscopy (AFM) (Cypher ES, Asylum Research, Oxford Instrument). The conducting Pt/Ir coated Si tip (Nanosensors, PPP-NCSTPt) was employed with a calibrated spring constant $k \sim 3.48$ N/m. The morphology and surface potential were collected in a non-contact mode. A UV-Vis spectrophotometer (Agilent Technologies, Cary Series) was used to analyze light absorption ability and estimate the bandgaps of all the samples. A FLS1000 spectrometer (Edinburgh Instruments, UK) was employed to collect transient-state photoluminescence (PL) spectra and a FLS980 spectrometer (Edinburgh Instruments, UK) was used for measurements of fluorescence and phosphorescence. Steady-state PL spectra were obtained on an RF-5301PC spectrofluorophotometer (Shimadzu, Japan). N₂ adsorption-desorption isotherms were acquired by a physisorption technique (ASAP 2460). Thermogravimetric analysis was performed on a Mettler Toledo thermogravimetric analyzer. Cross-polarization (CP) magic-angle spinning nuclear magnetic resonance (MAS NMR) spectra was collected on a Varian VNMRs WB spectrometer (¹³C 100.554 MHz) equipped with a 4 mm MAS probe. Electron paramagnetic resonance (EPR) spectra with in situ light irradiation were acquired on a Bruker A300–10/12, employing a 500 W Xenon lamp (Newport) as the light source. Near edge X-ray absorption fine structure (NEXAFS) tests were carried out with the Soft-X-ray beamline from the Australian Synchrotron. Element analysis was carried out on an Elementar Vario EL cube. The mineralization degree of wastewater was analyzed on a Shimadzu total organic carbon (TOC) analyzer.

2.5. Photodegradation tests

Photodegradation performance of naproxen on the prepared photocatalysts was evaluated in a customized reactor under visible light irradiation (500 W Xenon lamp, Newport). Specifically, 3 mg of photocatalyst was dispersed into 50 mL naproxen aqueous solution (20 mg/L) in a 150 mL round-bottom double jacket reactor (diameter 50 mm, temperature maintained at 25 °C via external water circulation), with

magnetic stirring at 300 rpm for 30 min in the dark to achieve the adsorption-desorption equilibrium. The photocatalysis was initiated using a 500 W Xenon arc lamp with a 420 nm cut-off filter for visible light illumination. The temperature of the reaction system was maintained at 25.0 ± 0.2 °C by circulating water between a double-walled quartz cooling jacket. At specific intervals, 1.5 mL suspension was extracted and filtered through a 0.22 μ m Millipore filter for analysis. The concentration of NPX was determined by an ultrahigh performance

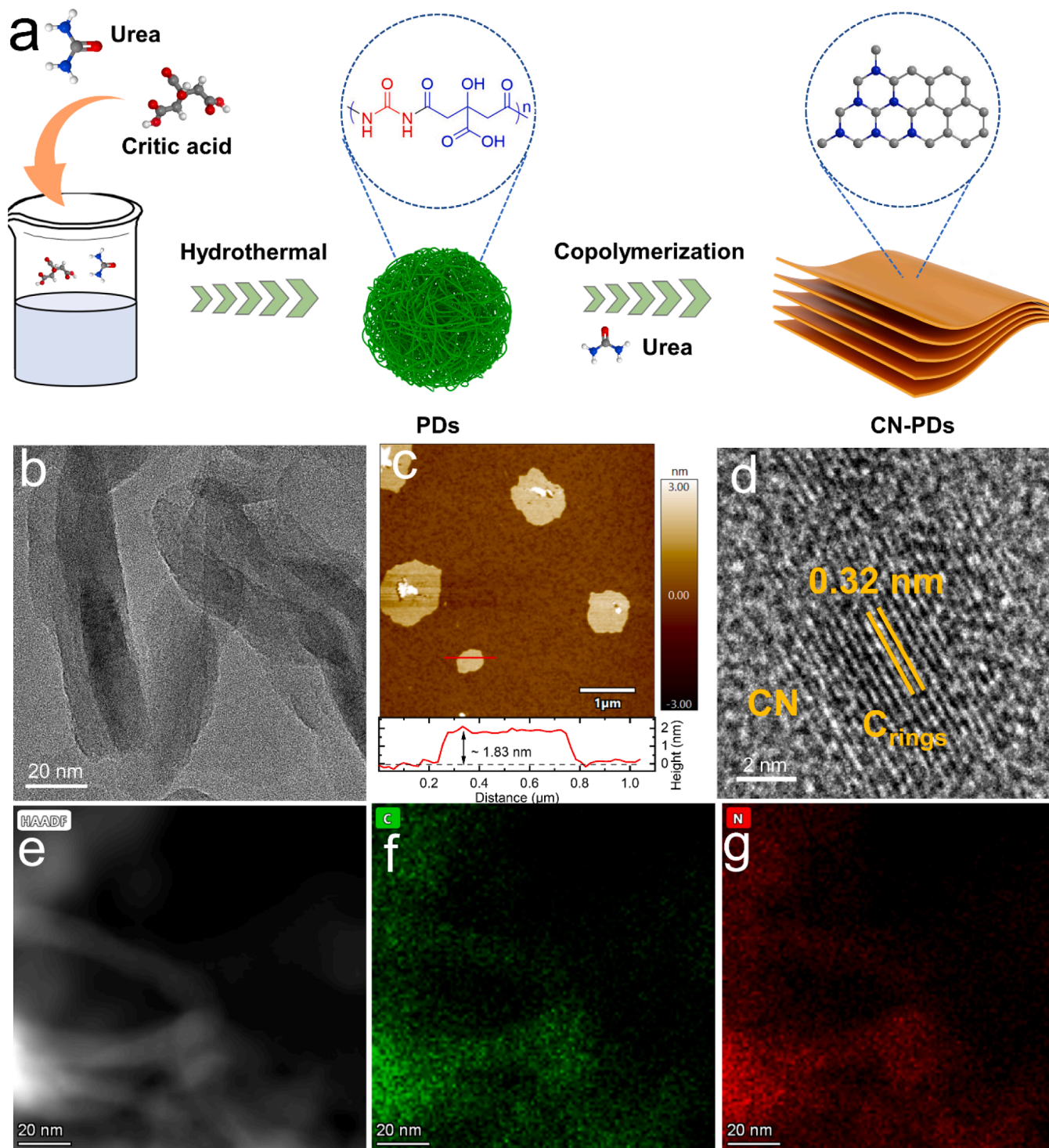


Fig. 1. Material synthesis and characterizations. (a) Illustration of synthesis of metal-free carbon/carbon nitride in-plane heterojunction. (b) TEM images. (c) AFM image and the corresponding thickness curves along the line (inset). (d) HRTEM image of CN-PDs_{0.1}. (e) HAADF-STEM image and (f-g) EDX elemental mapping images of CN-PDs_{0.1}.

liquid chromatograph (UHPLC, Thermo scientific 3000) with a C18 column and a UV detector (at 235 nm). The same methodology was applied for the photodegradation assessment of other pollutants, substituting NPX with SMX, IBP, BPA, BA, 4-CP, ACV, and ACP, respectively. The catalyst was subjected to three cycles of photodegradation testing with NPX for stability assessment, and after each cycle, it was cleaned using ultrasonic treatment with ethanol and pure water. The photodegradation performance was also evaluated in real wastewater, with hydrochloric acid and sodium hydroxide used to control the pH of the reaction aqueous solution.

2.6. Photoelectrochemical measurements

Photocurrent assessments, Mott-Schottky analyses, and electrochemical impedance spectroscopy (EIS) measurements were conducted using a CHI 760E electrochemical workstation (CH Instruments, Inc, USA). The synthesized sample was coated onto a glassy carbon electrode (GCE) for the fabrication of working electrode. A Pt wire was utilized as the counter electrode, while an Ag/AgCl electrode was employed as the reference electrode. 0.5 M of Na₂SO₄ solution was used as the electrolyte. To prepare the working electrode, 5 mg of photocatalyst was dispersed in a 500 μ L ethanol solution containing 20 μ L of Nafion 117 solution. The resultant slurry was subsequently coated onto the surface of GCE. The working electrode was obtained after natural drying for three days. A Xenon lamp (Aulight CEL-PF300-T8) was employed as the light source. The illuminated area on the working electrode covered 1 cm². An examination for the Mott-Schottky plots was performed across a voltage spectrum spanning from -2 to -0.2 V in relation to Ag/AgCl reference, with the amplitude of 0.01 V and the frequency of 6, 7, and 8 kHz, respectively.

3. Results and discussions

3.1. Catalyst preparation and characterizations

The synthetic process of carbon ring/carbon nitride planar heterojunction (CN-PDs_x) is illustrated in Fig. 1a. Polymer dots (PDs) were synthesized by a hydrothermal method using urea and citric acid as precursors. The carboxyl groups of citric acid molecules reacted with amino groups of urea for acylamino groups in the resultant PDs (Fig. S1). PDs were then mixed and copolymerized with urea at a medium-high temperature (600 °C). Terminal amino and carboxyl groups on the surface of PDs adsorbed urea molecules, which directionally grew along the carbonated matrix of PDs in polymerization process for CN-PDs_x. As such, a lateral heterostructure integrated of carbocycles and tri-s-triazine rings is acquired as a promising metal-free photocatalyst [27].

To observe the fabrication process of CN-PDs_x lateral heterojunction, transmission electron microscopy (TEM) images of PDs were captured, displaying well-defined, monodispersed and uniformly distributed nanospheres with an average diameter of 23 nm (Figs. S2–3). PDs are different from carbon quantum dots as they are unstable under the attack of high energy electron beam owing to the low polymerization degree. TEM images depict the process of structure degradation of PDs (Fig. S2a–d), showing the transformation from solid spheres to hollow shells. TGA results also confirm that PDs can be easily decomposed by 60 % when the temperature rises to 125 °C (Fig. S4). Consequently, PDs possess a more extensive π -conjugated structure compared to small organic molecules yet exhibit lower stability than carbon dots. After the copolymerization of PDs with urea at 600 °C, clear lamellar stacking nanosheets with a thickness of 1.83 nm can be observed for CN-PDs_{0.1}, where PDs in the nanosphere structure disappeared (Fig. 1b–c). Compared to pristine CN, the ultra-thin nanosheets in CN-PDs_{0.1} remain, which show enlarged planar structure after the introduction of PDs during the urea polymerization process (Fig. S5). This observation indicates that the carbocycles present in PDs play a key role in promoting the epitaxial growth of tri-s-triazine rings, fostering the formation of

carbon/carbon nitride in-plane heterojunctions.

Distinct lattice fringe regions can be observed from HRTEM image for CN-PDs_{0.1} (Fig. 1d), which are incorporated into the basal plane of CN. The lattice spacing is estimated to be 0.32 nm, attributed to the interlayer stacking distance of graphene [28,29]. Besides, we fail to find obvious boundaries or interfaces between the carbon nitride and inserted carbocycles (Fig. 1d), indicating the random assembly of carbon rings and carbon nitride matrix into a planar heterostructure. Furthermore, elemental mapping images of CN-PDs_{0.1} display that the thin lateral heterojunction is primarily comprised of C and N elements (Fig. 1e–g), which are unevenly distributed on CN-PDs_{0.1} as evidenced by the different C/N ratios at the two selected positions (Fig. S6), illustrating the existence of heterojunction across the two-dimensional plane.

We also utilized Fourier transform infrared (FTIR) spectra to confirm the incorporation of carbon rings into the basal plane of carbon nitride. Acylamino groups at 1664 cm⁻¹ can be found in the FTIR spectra of PDs, confirming the polymerization of citric acid and urea for the polymer dots (Fig. S7) [30]. Meanwhile, terminal carboxyl and amino groups exist on the surface of PDs [30], which serve as active sites for the epitaxial growth of carbon nitride along PDs. The incorporation of PDs into the carbon nitride matrix leads to a change in the vibrational bands in the FTIR spectra. After the copolymerization of PDs and urea, the intensity of the vibration bands at 806, 1000–1700, and 3000–3400 cm⁻¹ (Fig. 2a), corresponding to the s-triazine unit, C–N stretching vibrations in CN heterocycles, and amino groups (N–H), respectively, gradually decrease with the increased number of PDs during the fabrication of CN-PDs_x. This indicates that the heptazine framework of CN alters along with the incorporation of π -conjugated carbon rings during the carbonation with PDs.

For analysis of the chemical structure in the resultant planar heterojunction, XRD patterns of the as-prepared samples were first collected (Fig. 2b). Carbon nitride exhibits two diffraction peaks at 13.1 and 27.5°, where the former (100) peak is assigned to the in-plane structural packing motif of tri-s-triazine units and the latter (002) peak originates from the interlayer-stacking structure [21]. By contrast, PDs show a broad (002) band of graphene as reported in the literature, indicating the generation of a graphene-derived structure but with a low graphitic/polymerization degree [31]. It should be noted that the intensity of the (100) peak gradually decreases at increased loading of PDs during the synthesis of CN-PDs_x. In addition, there is a slight upshift of the (002) peaks in the lateral heterojunction (Fig. 2c), suggesting the laterally periodic tri-s-triazine structure of carbon nitride is partially destroyed by the incorporated carbon rings [31,32].

Solid-state ¹³C NMR measurements were performed to substantiate the molecular structure before and after the insertion of carbocycles into the carbon nitride matrix. As illustrated in Fig. 2d, both CN and CN-PDs_{0.1} show two apparent peaks at approximately 162 and 154 ppm, which are the representative assignments of CN₃ groups (C₁) in heptazine rings and carbon atoms adjacent to the amino group (C₂) in the heptazine units of CN, respectively [33,34]. Additionally, a peak appears at 116 ppm for CN-PDs_{0.1}, ascribing to aromatic C=C (C₃) [35], proving the formation of carbon rings after the copolymerization of PDs and urea. The implant of carbon rings into carbon nitride basal plane is further confirmed by elemental analysis (EA). The C/N ratio presented in Table S1 increases from 0.57 to 0.68 when the dosage of PDs in the fabrication of lateral heterojunction increases from 0 to 0.5 g, indicating a controllable content of carbocycles in the resultant CN-PDs_x samples. Therefore, PDs are proven to be an optimal precursor for fabricating carbon ring/carbon nitride lateral heterojunction.

Near-edge X-ray absorption fine structure (NEXAFS) spectra were acquired to gain insight into the chemical structures of all samples. Peaks at 287.2 and 288.4 eV in carbon K-edge spectra (Fig. 2e) are assigned to the C=C and C=N–C resonances, respectively. Two typical characteristic resonances at 399.4 and 402.3 eV in the nitrogen K-edge region (Fig. 2f) correspond to the C–N–C coordination in CN units and N–

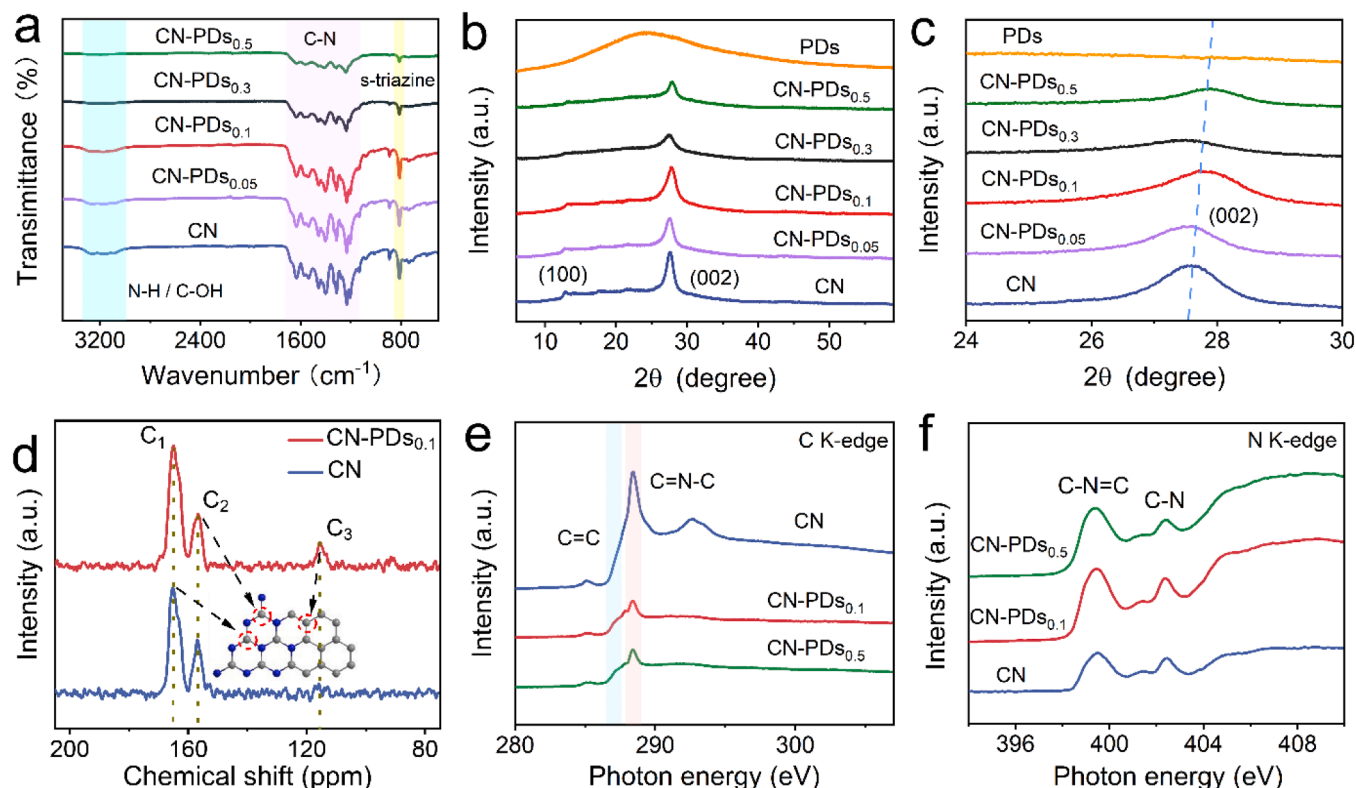


Fig. 2. Characterizations of CN and CN-PDs_x. (a) FTIR spectra, (b) XRD patterns, and (c) amplifying XRD patterns between 24° and 30° for synthesized samples. (d) Solid-state ¹³C NMR spectra for CN and CN-PDs_{0.1}, and NEXAFS results of (e) C K edge and (f) N K edge for CN, CN-PDs_{0.1} and CN-PDs_{0.5}.

3C bridging among three tri-s-triazine rings, respectively [35]. Compared with CN, we observed the appearance of C=C peak for CN-PDs_{0.1} and CN-PDs_{0.5}, indicating the creation of carbon rings in CN-PDs_x. X-ray photoelectron spectroscopy (XPS) confirms the results of NEXAFS (Fig. S8). The XPS survey spectra show that CN, CN-PDs_{0.1} and CN-PDs_{0.5} are primarily composed of C and N elements. As shown in C 1 s spectra (Fig. S8a), the fitted peaks at 284.8 and 288.3 eV are indexed to the C-C/C=C bond and triazine rings (N-C=N) [36], respectively. The N-C=N peak downshifts after the modification by carbon rings. Interestingly, the peak areas of C-C/C=C peak is remarkably higher for CN-PDs_{0.1} and CN-PDs_{0.5} than that for pristine CN, revealing the successful incorporation of graphitic carbon rings into the CN framework. A similar trend to the C 1 s spectra is also witnessed in the N 1 s spectra (Fig. S8b), where three fitted N peaks at 398.7, 399.9, and 401.2 eV are assigned to the C=N-C, N-(C)-, and C-NH, respectively [37]. These peaks all shift to lower binding energies with the creation of the lateral heterostructure in CN-PDs_{0.5}. As a result, the various characterizations in the study confirmed the successful incorporation of carbon rings into the carbon nitride matrix when PDs are introduced in the fabrication process.

3.2. Physicochemical properties

Nitrogen adsorption and desorption isotherms were collected to study SSAs and pore structures of all the prepared samples (Fig. S9a). CN-PDs_{0.05} and CN-PDs_{0.1} demonstrate lower SSAs than other samples, attaining 71.6 and 64.6 m²/g, respectively. Further increasing the dosage of PDs in the fabrication process of lateral heterostructure results in a larger SSA, as demonstrated by values of 84.2, 90.8 and 90.0 m²/g for CN, CN-PDs_{0.3} and CN-PDs_{0.5}, respectively (Fig. S9b). The pore volume and pore size were determined by pore distribution curves (Fig. S9c), where mesoporous structures are dominant for all the samples.

Prior to the evaluation of their photocatalytic activities, the light

absorption properties and photo-induced charge dynamics were assessed for all the samples. UV-Vis diffuse reflectance spectra (Fig. 3a) show a prominent tail, suggesting a significant enhancement in visible light absorption over the in-plane heterojunction. The marginal absorption edges of CN, CN-PDs_{0.05} and CN-PDs_{0.1} are at 440, 460 and 520 nm, respectively, illustrating that more carbocycles in the CN-PDs_x lead to intensified light responses. Furthermore, the light response upon CN-PDs_{0.3} and CN-PDs_{0.5} even extends to the near infrared region. Based on the data collected, the band gap energy (E_g) was estimated to be 2.68 eV for CN, 2.60 eV for CN-PDs_{0.05}, 2.40 eV for CN-PDs_{0.1}, 1.0 eV for CN-PDs_{0.3} and 0.5 eV for CN-PDs_{0.5} (Fig. S10). This suggests an approaching conductor property with more aromatic carbon rings embedded in the lattice. The valence positions of 1.58, 1.51, 1.40, 1.37, and 1.36 eV for CN, CN-PDs_{0.05}, CN-PDs_{0.1}, CN-PDs_{0.3} and CN-PDs_{0.5}, respectively, were determined from XPS VB spectra (Fig. S11). Furthermore, Mott-Schottky curves at different frequency were obtained to estimate the conduction band (CB) positions of CN and CN-PDs_{0.1}, which were determined to be -1.1 and -1.0 eV, respectively (Fig. S12) [23]. As such, the band structures of pristine CN and CN-PDs_{0.1} were locked in Fig. S13.

The dynamics of photo-induced charge carriers were then investigated for all the samples. First, PL spectra were used to study the separation rate of photo-excited electron-hole pairs (Fig. 3b). When excited at the wavelength of 325 nm, pristine CN displays a strong emission peak at approximately 460 nm. The peak intensity is the highest among all the samples, indicating the fastest recombination rate of electron-hole pairs. Noticeably, PL peak intensity gradually decreases with the increased density of carbon rings in CN-PDs_x, demonstrating that carbon motifs within the CN matrix significantly accelerate charge separation and decrease the recombination rate of e⁻ and h⁺ pairs. In addition, the fluorescence lifetimes of CN and CN-PDs_x samples are acquired to analyze photo-induced charge dynamics (Fig. 3c). Photo-excited hot electrons exhibit the longest lifetime of 1.33 ns in CN, which is longer than CN-PDs_{0.3} (0.26 ns). The lifetime of the photo-excited charge

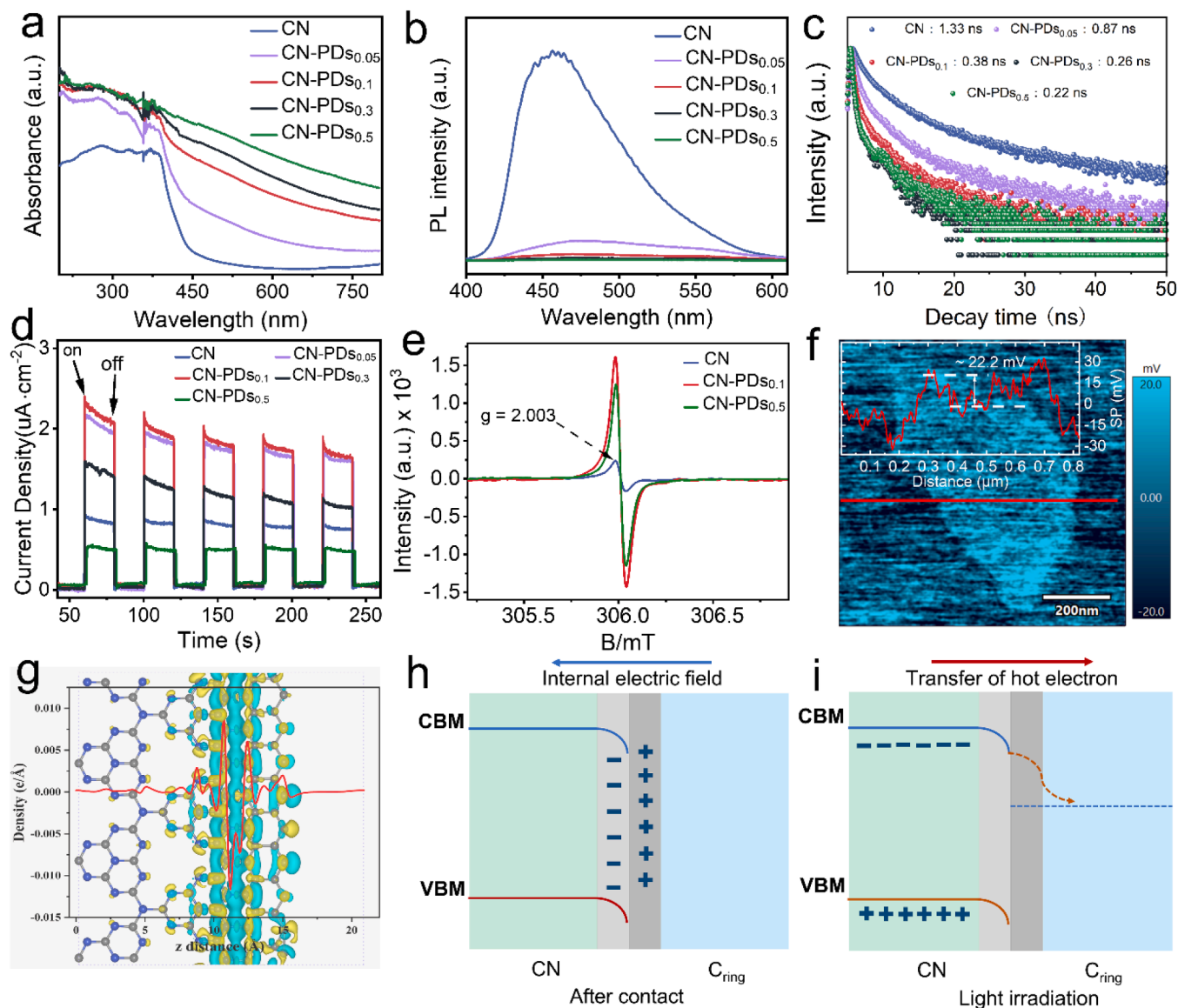


Fig. 3. Optoelectrical properties. (a) UV-Vis absorption spectra. (b) PL spectra. (c) Time-resolved transient PL decay. (d) Photo-current response. (e) Solid EPR spectra of CN and CN-PDs_x samples. (f) KPFM image of CN-PD_{0.1}. (g) Planar averaged charge density difference along the z-direction for CN-PD_{0.1}. (h) Created internal electric field (IEF) at the contact between CN and carbon rings. (i) IEF assisted charge separation in CN-PD_{0.1} under light irradiation.

carriers decreases as more PDs were introduced in the fabrication of lateral heterojunction, as illustrated by the lifetime of 0.87, 0.38, and 0.22 ns for CN-PDs_{0.05}, CN-PDs_{0.1}, and CN-PDs_{0.5}, respectively. The shorter transient fluorescence decay lifetime (τ) is related to exciton radiative decay from the conduction band to the valence band. Incorporating carbon rings in the carbon nitride matrix can enhance the separation and transfer of photo-excited charge carriers by efficiently trapping the photogenerated electrons, resulting in a shorter fluorescence decay lifetime (τ).

Furthermore, the enhanced photo-induced charge dynamics in the lateral heterostructure is further verified by the photoelectrochemical measurements. A photocurrent response is recorded to assess the separation and transportation efficiency of photo-induced charge carriers. It can be obviously observed that the photocurrent for CN-PDs_x sharply increases compared to pristine CN, indicating a higher charge separation rate after carbon rings grow along the CN basal plane (Fig. 3d). The EIS plots also suggest that CN has the largest radius among all the obtained materials, indicating its higher interface impedance resistance. On the other hand, the addition of more carbon rings in CN-PDs_x remarkably

lowers the interface impedance resistance, thus promoting the migration of photogenerated charge carriers (Fig. S14) [38]. EPR spectra confirm the enhanced charge dynamics in CN-PDs_x, as the paramagnetic signal at a g factor of 2.003 is ascribed to the unpaired electrons. CN-PDs_{0.1} and CN-PDs_{0.5} show higher EPR peaks than CN (Fig. 3e), indicating the addition of carbon rings into carbon nitride supplies extra charges for photo-excitation and subsequent surface redox reactions [39]. Based on the above results, conclusions can be reached that the electronic structure of CN matrix has been optimized via the insertion of carbon ring, leading to efficient photoexcited carrier's generation, electron-hole separation and fast charge migration dynamics.

To elucidate the enhanced charge dynamics after the fabrication of in-plane heterojunction, Kelvin probe force microscopy (KPFM) technology provides quantitative results of the local surface potential distribution of conductive or semiconductive samples, thus was applied to study the electrical surface properties of CN-PDs_{0.1}. Results in Fig. 3f revealed that the surface potential on CN-PDs_{0.1} is not homogeneous. The central regions of the flake present a higher potential, which supports the presence of an enhanced internal electric field (IEF) within the

lateral heterojunction to promote the separation and transportation of photo-excited electron-hole pairs.

DFT simulation is further conducted to gain insights into the promoted charge dynamics in the in-plane heterojunction (Fig. S15). Simulation results indicate that the electrons at the interface of CN-PDs_{0.1} experience significant re-arrangement and re-localization, leading to the transfer of electrons from the graphite carbon region to the CN region (as revealed from the red line in Fig. 3g) [40,41]. This creates an IEF between the two regions, with the IEF pointing from the graphite carbon to the CN region (Fig. 3h). The IEF facilitates the separation of photo-induced electrons generated on the CN region under visible-light irradiation, driving them towards the carbon rings (Fig. 3i) [34,35]. The existence of IEF is further confirmed by the variation in the charge density profile along different directions. CN and graphite carbon display symmetrical structures, and their average charge densities exhibit periodic variations in x and y directions (Fig. S16a-f). However, when CN units and carbon rings contact, the molecular structure in x direction turns evidently asymmetrical, while the change of charge density keeps a periodic trend, indicating that the created IEF by the implanted carbon rings promotes charge re-distribution in CN-PDs_x (Fig. S16g-i). As a result, the transportation dynamics of photo-excited charges can be remarkably enhanced across the in-plane heterojunction.

3.3. Photodegradation performance

NPX was chosen as the target pollutant to evaluate the photodegradation performance of all the metal-free photocatalysts under visible light irradiation. In the absence of catalysts, no appreciable change in NPX concentration was observed after 60-min visible light irradiation (blank line in Fig. 4a), indicating the neglectable self-photolysis of NPX. A 90-minute adsorption experiment was conducted for NPX in the absence of light irradiation. The concentration of NPX stops descending after 30 min, reaching the adsorption-desorption equilibrium (Fig. S17).

Photodegradation process is initiated upon activation of visible light. Using pristine CN, the photodegradation efficiency of NPX is lower, with only approximately 45 % of NPX removal within 60 min of light irradiation. The lower photodegradation efficiency observed with pristine CN can be largely attributed to sluggish charge generation and separation dynamics and a small SSA. Implanting carbon rings into the carbon nitride basal plane leads to improved photocatalytic activity for NPX removal in the aqueous solution. In detail, the NPX removal efficiencies for CN-PDs_{0.05}, CN-PDs_{0.1}, CN-PDs_{0.3} and CN-PDs_{0.5} are 100 %, 100 %, 80 % and 45 %, respectively. CN-PDs_{0.1} with an optimal content of immobilized carbocycles exhibits the highest photocatalytic activity, while further improving the PD amount during the synthesis results in declined photocatalytic activity. This is because more carbon rings would destroy the semiconducting property of carbon nitride and result in less production of energetic hot carriers upon light irradiation, which cannot be compensated by the improved charge migration dynamics due to enhanced conductivity (Fig. S10 and 14) [42].

It's worth noting that the activity of the catalyst strongly depends on the rate of photon absorption within the reactor, and this rate can vary depending on the catalyst concentration and the specific catalyst specimens used. Therefore, to support these conclusions, various optical parameters of the catalysts, including absorption and scattering coefficients, reactor thickness, and the total rate of photon absorption, were evaluated [43–45]. In this context, Fig. S18a demonstrates that the type of catalyst has a minimal impact on photon absorption intensity. Moreover, optical thickness emerges as a critical factor in determining photocatalytic performance. Consequently, the optical thicknesses of different catalysts were calculated and found to be 3.27, 4.91, 6.86, 4.19, and 3.50 for CN, CN-PDs_{0.05}, CN-PDs_{0.1}, PDs_{0.3}, and PDs_{0.5}, respectively. To ensure a meaningful comparison between the catalysts, experiments were also conducted at equal optical thickness. The results, as shown in Fig. S18b, indicate that the contribution of optical thickness from different carbon nitride-based catalysts to the photodegradation of NPX can be considered negligible.

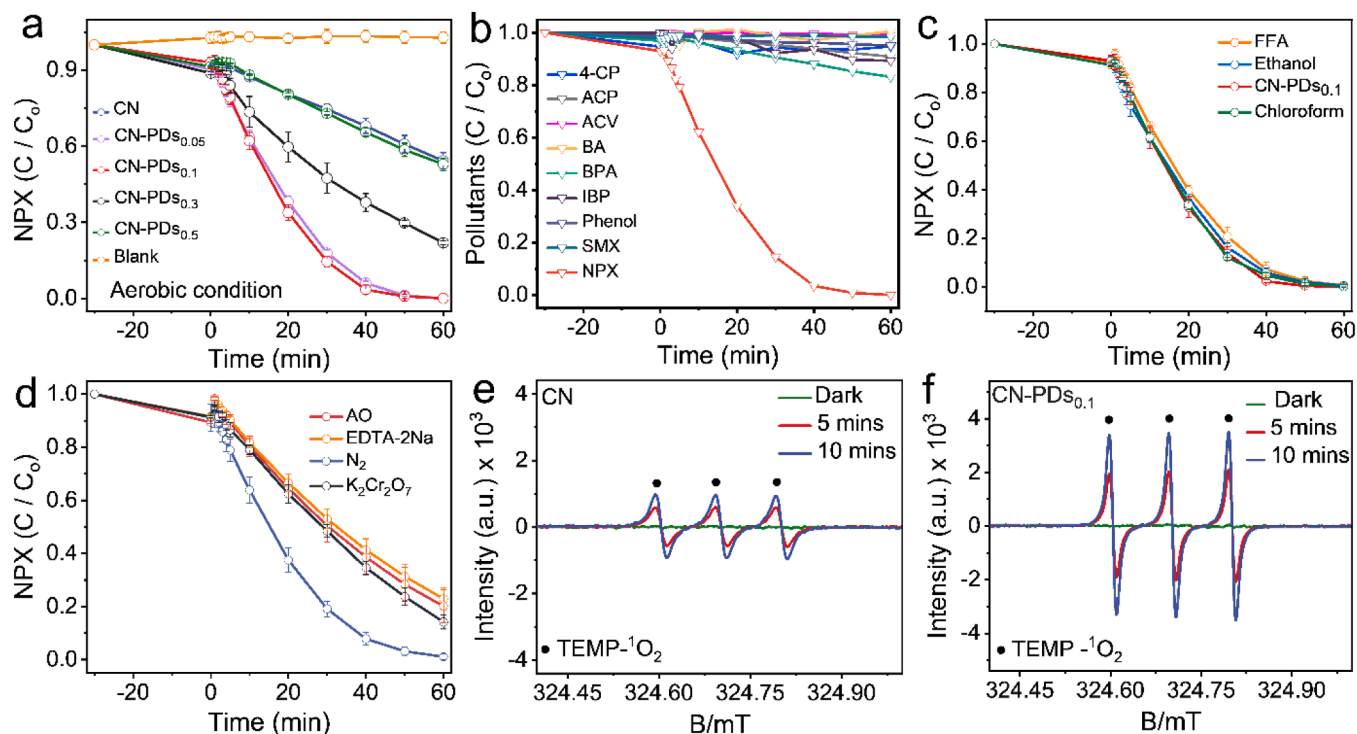


Fig. 4. Photodegradation performance. (a) NPX photodegradation efficiency by CN and CN-PDs_x. (b) Photodegradation of different pollutants using CN-PDs_{0.1} as photocatalyst, concentration of pollutant: 20 mg/L. (c-d) Trapping experiments of CN-PDs_{0.1} based photodegradation of NPX with different scavengers. Catalyst amount: 0.06 g/L; Naproxen concentration: 20 mg/L; concentration of scavengers: [EtOH]₀ = 2 mM; [NaN₃]₀ = 1 mM; [AO]₀ = 1 mM; [EDTA-2Na]₀ = 1 mM; [K₂Cr₂O₇]₀ = 1 mM; [Chloroform]₀ = 5 mM; FFA = 4 mM. (e-f) EPR measurements for singlet oxygen in photodegradation of NPX on CN and CN-PDs_{0.1}.

The kinetic rate constants for the prepared samples in photodegradation of NPX are presented to compare their photocatalytic performances. Pseudo-first order kinetic curves are revealed for all the samples in the photodegradation process (Fig. S19–20). The kinetic rate constant for CN-PDs_{0.1} is 0.053 min⁻¹, which is 5.3 or 5.8 times greater than that of CN-PDs_{0.05} and CN, respectively. Notably, CN-PDs_{0.1} also outperforms state-of-the-art CN-based catalysts in NPX photodegradation, underscoring the efficiency of constructing carbon/carbon nitride in-plane heterojunctions to enhance charge dynamics and improve photodegradation performance (Table S2). Furthermore, the photodegradation performance of CN-PDs_{0.1} was evaluated for other pollutants, revealing negligible removal efficiency in contrast to the effective NPX photodegradation (Fig. 4b). In addition, the effect of pH variation, spanning from 3 to 11, was examined, leading to a gradual reduction in degradation efficiency as pH increased (Fig. S21a). Similarly, noticeable decreases were observed in the photodegradation efficiency of NPX in ultrapure water for CN-PDs_x under near-neutral conditions (Fig. S21b). The reason behind the high NPX photodegradation performance in acidic solutions and the lower performance in neutral and alkaline environments lies in its protonation and deprotonation processes. Under acidic conditions, the NPX can become protonated due to the formation of H⁺ ions [46–48], thereby improving the charge dynamics, and consequently, the improved photodegradation activity. Conversely, in neutral or alkaline environments, the NPX undergoes deprotonation, which hinders its adsorption onto catalyst (under alkaline condition) and resistance against ROS and the photo-reduction pathway. Therefore, nearly complete removal of NPX in tap and river water was achieved by adjusting the pH values of their aqueous solutions to 4.6 (Fig. S22), showcasing the practical applicability of the NPX photodegradation process. Moreover, the stability of CN-PDs_{0.1} slightly decreased from 100 % to 97 % after three cycles of testing (Fig. S23), and 45 % of TOC removal was achieved during the NPX photodegradation (Fig. S24).

3.4. Reactive species detection and reaction mechanism

To clarify the reaction mechanism of the photodegradation of NPX, we conducted quenching experiments to monitor various reactive species. As shown in Fig. 4c–d, the photocatalytic activities remain unaffected after adding ethanol and chloroform as quenchers for $\bullet\text{OH}$ and $\text{O}_2^{\bullet-}$, respectively. The results suggest that $\bullet\text{OH}$ and $\text{O}_2^{\bullet-}$ are not responsible for the degradation of NPX. However, when $\text{K}_2\text{Cr}_2\text{O}_7$ was added to the photodegradation system, the kinetic rate constant for NPX degradation decreased from 0.053 to 0.03 min⁻¹ (Fig. S25). Since $\text{K}_2\text{Cr}_2\text{O}_7$ is a typical electron trapping agent, the reduced photocatalytic performance suggests that photo-induced hot electrons are responsible for the photodegradation of NPX.

In addition, adding AO and EDTA-2Na resulted in declined kinetic rate constant from 0.053 min⁻¹ (control group) to 0.02 and 0.03 min⁻¹, respectively (Fig. S25b). These findings demonstrate that photo-excited e^- and h^+ are also involved in the photodegradation of NPX. Furthermore, we introduced FFA as a specific quencher of $^1\text{O}_2$ into the photocatalytic system (Fig. 4c). The results indicate the involvement of $^1\text{O}_2$ in the photocatalytic degradation process, as the NPX removal rate decreased from 0.053 to 0.039 min⁻¹ upon the addition of FFA (Fig. S25a). The activation of $^1\text{O}_2$ by CN-PDs_{0.1} under visible light irradiation was also confirmed by EPR measurements (Fig. 4e–f), where a characteristic signal with a peak ratio of 1:1:1 (ascribed to $^1\text{O}_2$) was observed after light irradiation. The results confirm that nonradical photodegradation involves photo-induced hot carriers and $^1\text{O}_2$, when using CN-PDs_x as photocatalysts for NPX removal. The nonradical photodegradation mechanism is consistent with the high selectivity and low stability in the degradation of organic pollutants [49,50].

To distinguish the contributions of $^1\text{O}_2$ and photo-excited high-energy carriers to the nonradical mechanism, the photodegradation of NPX was performed under an anaerobic condition. As depicted in Fig. 5a, the removal efficiencies of CN and CN-PDs_{0.5} under 60-min visible light irradiation were 30 % and 28 %, respectively. In addition, 95 %, 100 %

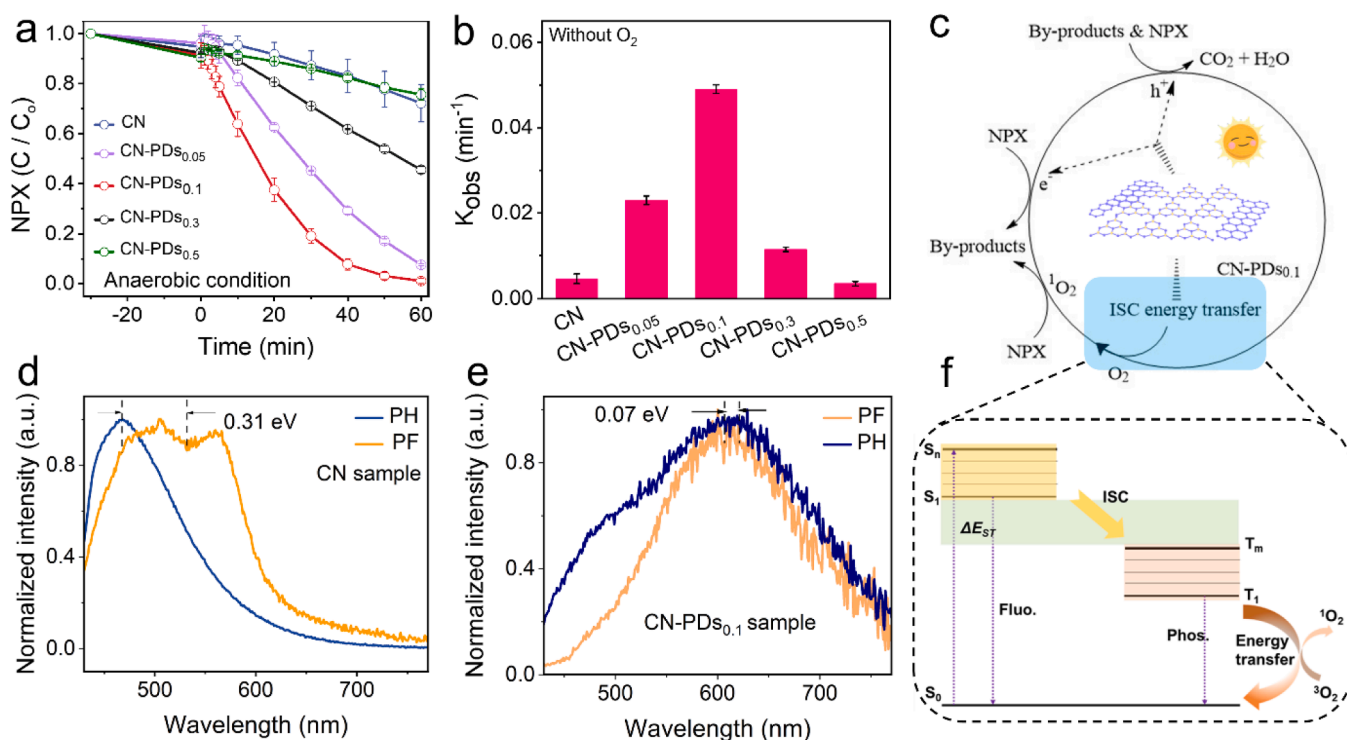


Fig. 5. Structure-performance relationships. (a) Anaerobic photodegradation efficiency for all of samples (N₂ purge). (b) Kinetic rate constants of anaerobic photodegradation for all of samples. Catalyst amount: 0.06 g/L; Naproxen concentration: 20 mg/L. (c) Proposed mechanism of NPX removal under the visible light irradiation conditions. (d–e) Normalized fluorescence (PF) and phosphorescence spectra (PH) of CN and CN-PDs_{0.1} at room temperature (excitation wavelength at 365 nm and delay time is 1 ms). (f) Diagram of the energy transfer process on CN-PDs_{0.1} for singlet oxygen.

and 50 % of NPX removal were achieved by CN-PDs_{0.05}, CN-PDs_{0.1} and CN-PDs_{0.3}, respectively. The first-order kinetic rate constants for all the catalysts slightly decreased under anaerobic conditions, compared to those in aerobic conditions (Fig. 5b), suggesting that reactive species (e.g., ¹O₂) generated from dissolved oxygen did not significantly contribute to photodegradation of NPX. Furthermore, the photodegradation rates of NPX significantly reduced upon additions of K₂Cr₂O₇ and EDTA-2Na, respectively (Fig. S26). Therefore, it can be concluded that photo-induced high-energy electrons and holes dominate the NPX removal, while singlet oxygen generated from oxygen makes a minor contribution to the nonradical photodegradation process. It is noteworthy that CN-PDs_{0.1} exhibits 100 % NPX removal efficiency under both aerobic and anaerobic conditions, rendering it as a highly efficient photocatalyst for wastewater treatment.

To gain insight into the NPX photodegradation pathway, we conducted an analysis of reaction intermediates using LC-MS. The LC-MS spectra revealed the presence of numerous fragments (Fig. S27), offering valuable clues. Building on these findings, a possible reaction mechanism can be proposed for the nonradical photodegradation process (Fig. 5c). In this mechanism, photo-generated high-energy electrons and holes as well as intersystem crossing (ISC) induced singlet oxygen collaboratively engage in the attack on NPX through electrophilic oxidation and electron transfer processes [51]. The degradation process of NPX comprises three possible pathways (Fig. S28). The initial pathway involves the cleavage of the carboxylic group of NPX, resulting in the generation of radicals through either photoexcited electrons (e⁻) or singlet oxygen (¹O₂) [52,53]. Following this step, a dehydrogenation or a ring opening process occurs, yielding intermediate products with mass-to-charge ratios (*m/z*) of 170, 185, and 221. After these intermediates, an oxidation process takes place, culminating in the creation of a ring-opening product that eventually mineralizes into H₂O and CO₂ [52]. In pathway 2, an attack by h⁺ directly targets NPX, inducing decarboxylation for the intermediate (*m/z* of 158), which experiences further oxidation for the formation of intermediates (*m/z* of 137 and 149), along with H₂O and CO₂, as a result of the ring-opening process [53]. Within pathway 3, NPX undergoes a de-etherisation process, producing an intermediate with an *m/z* value of 201 due to h⁺ oxidation. This intermediate, however, fails to be further oxidized. This observation correlates with the TOC results, indicating that specific components of NPX were mineralized into H₂O and CO₂, while others were transformed into organic by-products [54].

3.5. Discussions

The activation of singlet oxygen on the planar heterojunction was studied. Because O₂^{•-} is not detected (Fig. 4c) and the degradation rate remains after adding the quenching agent of ethanol, it can be indirectly inferred that ¹O₂ is not generated by an electron transfer mechanism, but via an energy-transfer pathway [19]. The singlet-triplet energy gap (ΔE_{st}) for CN and CN-PDs_{0.1} was determined using fluorescence (fluo.) and phosphorescence (phos.) lifetimes to estimate the efficiency of the intersystem crossing (ISC) process. The values of ΔE_{st} were calculated to be 0.07 and 0.31 eV for CN-PDs and CN, respectively (Fig. 5d-e). This suggests that the immobilization of carbon rings into carbon nitride matrix enables a better triplet-triplet energy transfer process, making the ISC process for easier production of singlet oxygen (Fig. 5f) [55]. Therefore, the relationship between the structure and performance of the planar heterostructure in the photodegradation of NPX can be revealed. The incorporated carbocycles into the lateral heterostructure significantly accelerate the electroconductivity, separation, and transfer of photo-induced hot carriers, resulting in the degradation of NPX via different pathways (Fig. 3c-e). Additionally, the carbon rings in the planar heterostructure decrease the barrier for intersystem crossing, resulting in improved energy transfer and direct oxygen activation and ultimately leading to the generation of ¹O₂ (Fig. 4e-f). As a result, the metal-free in-plane heterojunction photocatalyst enables fast charge and

energy transfer, leading to enhanced photodegradation of NPX. The photocatalysis harnesses oxidative holes, hot electrons, and singlet oxygen for nonradical oxidation.

4. Conclusion

In summary, polymer dots were innovatively utilized to fabricate metal-free carbon/carbon nitride in-plane heterostructures. The low carbonization degree and large π -conjugated structure enabled CN as a great substrate to build a resultant lateral heterojunction with controllable contents of carbon rings. The incorporated carbocycles significantly expedited the separation and transportation of photo-excited charge carriers in carbon nitride. Meanwhile, the incorporation of aromatic rings significantly reduced the energy barrier of ISC, enabling enhanced energy-transfer-mediated oxygen activation to produce ¹O₂ without involving radical oxygen species. As a result, the photodegradation of NPX was achieved through the combined action of reactive h⁺, e⁻, and ¹O₂. This work presents a new type of metal-free plane heterostructure photocatalysts for the purification of antibiotics from water through state-of-the-art nonradical oxidation.

CRediT authorship contribution statement

Yu Yao: *Conceptualization, Methodology, Writing-Original Draft, Validation.* Yantao Wang: *Data curation.* Teng Lu: *Data curation, Investigation.* Jinqiang Zhang: *Conceptualization, Writing-Review & Editing, Visualization.* Huayang Zhang: *Formal analysis.* Kunsheng Hu: *Data curation, Investigation.* Tara Pukala: *Resources.* Yun Liu: *Resources; Formal analysis.* Xiaoguang Duan: *Conceptualization, Supervision, Writing Review & Editing, Funding acquisition.* Shaobin Wang: *Supervision, Writing-Review & Editing, Funding acquisition.*

Declaration of Competing Interest

The authors declare that they have no known competing financial interests or personal relationships that could have appeared to influence the work reported in this paper.

Data availability

Data will be made available on request.

Acknowledgments

The authors acknowledge the financial support from the Australian Research Council under DECRA Scheme (DE210100253), merits SXR beamline from Australian Nuclear Science and Technology Organisation (ANSTO, AS231/SXR/19680), and computing resources provided by Australian Computational Infrastructure (NCMAS-2023-78).

Appendix A. Supporting information

Supplementary data associated with this article can be found in the online version at doi:10.1016/j.apcatb.2023.123363.

References

- [1] Q.G. Fu, T. Malchi, L.J. Carter, H. Li, J. Gan, B. Chefetz, Pharmaceutical and personal care products: from wastewater treatment into agro-food systems, *Environ. Sci. Technol.* 53 (2019) 14083–14090.
- [2] C. Xu, L. Niu, H. Guo, X. Sun, L. Chen, W. Tu, Q. Dai, J. Ye, W. Liu, J. Liu, Long-term exposure to the non-steroidal anti-inflammatory drug (NSAID) Naproxen causes thyroid disruption in zebrafish at environmentally relevant concentrations, *Sci. Total. Environ.* 676 (2019) 387–395.
- [3] M. Manrique-Moreno, M. Suwalsky, F. Villena, P. Garidel, Effects of the nonsteroidal anti-inflammatory drug naproxen on human erythrocytes and on cell membrane molecular models, *Biophys. Chem.* 147 (2010) 53–58.

- [4] J. Wang, X.G. Duan, J. Gao, Y. Shen, X.H. Feng, Z.J. Yu, X.Y. Tan, S.M. Liu, S. B. Wang, Roles of structure defect, oxygen groups and heteroatom doping on carbon in nonradical oxidation of water contaminants, *Water Res.* 185 (2020), 116244.
- [5] D. Wojcieszynska, U. Guzlik, Naproxen in the environment: its occurrence, toxicity to nontarget organisms and biodegradation, *Appl. Microbiol. Biotechnol.* 104 (2020) 1849–1857.
- [6] J. Kang, H. Zhang, X. Duan, H. Sun, X. Tan, S. Liu, S. Wang, Magnetic Ni-Co alloy encapsulated N-doped carbon nanotubes for catalytic membrane degradation of emerging contaminants, *Chem. Eng. J.* 362 (2019) 251–261.
- [7] J. Wang, X. Duan, J. Gao, Y. Shen, X. Feng, Z. Yu, X. Tan, S. Liu, S. Wang, Roles of structure defect, oxygen groups and heteroatom doping on carbon in nonradical oxidation of water contaminants, *Water Res.* 185 (2020), 116244.
- [8] X.G. Duan, H.Q. Sun, S.B. Wang, Metal-free carbocatalysis in advanced oxidation reactions, *Acc. Chem. Res.* 51 (2018) 678–687.
- [9] Y. Yao, H.Y. Zhang, K.S. Hu, G. Nie, Y.Y. Yang, Y.X. Wang, X.G. Duan, S.B. Wang, Carbon dots based photocatalysis for environmental applications, *J. Environ. Chem. Eng.* 10 (2022), 107336.
- [10] G. Chen, Y. Yu, L. Liang, X. Duan, R. Li, X. Lu, B. Yan, N. Li, S. Wang, Remediation of antibiotic wastewater by coupled photocatalytic and persulfate oxidation system: a critical review, *J. Hazard. Mater.* 408 (2021), 124461.
- [11] F. Zhao, Y. Liu, S.B. Hammouda, B. Doshi, N. Guijarro, X. Min, C.-J. Tang, M. Sillanpää, K. Sivula, S. Wang, MIL-101(Fe)/g-C₃N₄ for enhanced visible-light-driven photocatalysis toward simultaneous reduction of Cr(VI) and oxidation of bisphenol A in aqueous media, *Appl. Catal. B: Environ.* 272 (2020), 119033.
- [12] F.M. Yavitt, T.E. Brown, E.A. Hushka, M.E. Brown, N. Gjorevski, P.J. Dempsey, M. P. Lutolf, K.S. Anseth, The effect of thiol structure on allyl sulfide photodegradable hydrogels and their application as a degradable scaffold for organoid passaging, *Adv. Mater.* 32 (2020), e1905366.
- [13] S.J. Wang, L. Chen, X.L. Zhao, J.Q. Zhang, Z.M. Ao, W.R. Liu, H. Wu, L. Shi, Y. Yin, X.Y. Xu, C.C. Zhao, X.G. Duan, S.B. Wang, H.Q. Sun, Efficient photocatalytic overall water splitting on metal-free 1D SWCNT/2D ultrathin C₃N₄ heterojunctions via novel non-resonant plasmonic effect, *Appl. Catal. B: Environ.* 278 (2020) 0926–3373.
- [14] B. Ai, X.G. Duan, H.Q. Sun, X. Qiu, S.B. Wang, Metal-free graphene-carbon nitride hybrids for photodegradation of organic pollutants in water, *Catal. Today* 258 (2015) 668–675.
- [15] S.K. Le, C.Z. Zhu, Y.W. Cao, P. Wang, Q.S. Liu, H.C. Zhou, C.X. Chen, S.B. Wang, X. G. Duan, V₂O₅ nanodot-decorated laminar C₃N₄ for sustainable photodegradation of amoxicillin under solar light, *Appl. Catal. B: Environ.* 303 (2022) 0926–3373.
- [16] C. Chen, W. Ma, J. Zhao, Semiconductor-mediated photodegradation of pollutants under visible-light irradiation, *Chem. Soc. Rev.* 39 (2010) 4206–4219.
- [17] F. Li, T. Huang, F. Sun, L. Chen, P. Li, F. Shao, X. Yang, W. Liu, Ferric oxide nanoclusters with low-spin Fe^{III} anchored g-C₃N₄ rod for boosting photocatalytic activity and degradation of diclofenac in water under solar light, *Appl. Catal. B: Environ.* 317 (2022), 121725.
- [18] X. Liu, F. Li, Y. Liu, P. Li, L. Chen, B. Li, T. Qian, W. Liu, Degradation of diclofenac in a photosensitization-like photocatalysis process using palladium quantum dots deposited graphite carbon nitride under solar light, *J. Environ. Chem. Eng.* 10 (2022) 22133437.
- [19] P. Gan, Y. Lu, Y. Li, W. Liu, L. Chen, M. Tong, J. Liang, Non-radical degradation of organic pharmaceuticals by g-C₃N₄ under visible light irradiation: The overlooked role of excitonic energy transfer, *J. Hazard. Mater.* 445 (2023), 130549.
- [20] Y. Wei, Y. Zhu, Y. Jiang, Photocatalytic self-cleaning carbon nitride nanotube intercalated reduced graphene oxide membranes for enhanced water purification, *Chem. Eng. J.* 356 (2019) 915–925.
- [21] J.Q. Zhang, Y.G. Li, X.L. Zhao, H.Y. Zhang, L. Wang, H.J. Chen, S.J. Wang, X.Y. Xu, L. Shi, L.C. Zhang, J.P. Veder, S.Y. Zhao, G. Nealon, M.B. Wu, S.B. Wang, H.Q. Sun, A hydrogen-initiated chemical epitaxial growth strategy for in-plane heterostructured photocatalyst, *ACS Nano* 14 (2020) 17505–17514.
- [22] Y.Z. Liu, H.Y. Zhang, J. Ke, J.Q. Zhang, W.J. Tian, X.Y. Xu, X.G. Duan, H.Q. Sun, M. O. Tade, S.B. Wang, OD MoS₂/2D g-C₃N₄ heterojunctions in Z-scheme for enhanced photocatalytic and electrochemical hydrogen evolution, *Appl. Catal. B: Environ.* 228 (2018) 64–74.
- [23] W. Che, W. Cheng, T. Yao, F. Tang, W. Liu, H. Su, Y. Huang, Q. Liu, J. Liu, F. Hu, Z. Pan, Z. Sun, S. Wei, Fast photoelectron transfer in C_{ring}-C₃N₄ plane heterostructural nanosheets for overall water splitting, *J. Am. Chem. Soc.* 139 (2017) 3021–3026.
- [24] L. Cheng, H. Zhang, X. Li, J. Fan, Q. Xiang, Carbon-graphitic carbon nitride hybrids for heterogeneous photocatalysis, *Small* 17 (2021), e2005231.
- [25] H.R.S. Abdellatif, G. Zhang, X.T. Wang, D.T. Xie, J.T.S. Irvine, J.P. Ni, C.S. Ni, Boosting photocatalytic oxidation on graphitic carbon nitride for efficient photocatalysis by heterojunction with graphitic carbon units, *Chem. Eng. J.* 370 (2019) 875–884.
- [26] M. Semeniuk, Z.H. Yi, V. Poursorkhabi, J. Tjong, S. Jaffer, Z.H. Lu, M. Sain, Future perspectives and review on organic carbon dots in electronic applications, *ACS Nano* 13 (2019) 6224–6255.
- [27] Y. Wang, X. Liu, J. Liu, B. Han, X. Hu, F. Yang, Z. Xu, Y. Li, S. Jia, Z. Li, Y. Zhao, Carbon quantum dot implanted graphite carbon nitride nanotubes: excellent charge separation and enhanced photocatalytic hydrogen evolution, *Angew. Chem. Int. Ed. Engl.* 57 (2018) 5765–5771.
- [28] J.Y. Qin, H.P. Zeng, Photocatalysts fabricated by depositing plasmonic Ag nanoparticles on carbon quantum dots/graphitic carbon nitride for broad spectrum photocatalytic hydrogen generation, *Appl. Catal. B: Environ.* 209 (2017) 161–173.
- [29] Q.L. You, Q.X. Zhang, M.B. Gu, R.J. Du, P. Chen, J. Huang, Y.J. Wang, S.B. Deng, G. Yu, Self-assembled graphitic carbon nitride regulated by carbon quantum dots with optimized electronic band structure for enhanced photocatalytic degradation of diclofenac, *Chem. Eng. J.* 431 (2022), 133927.
- [30] W. Liu, Y.Y. Li, F.Y. Liu, W. Jiang, D.D. Zhang, J.L. Liang, Visible-light-driven photocatalytic degradation of diclofenac by carbon quantum dots modified porous g-C₃N₄: mechanisms, degradation pathway and DFT calculation, *Water Res.* 150 (2019) 431–441.
- [31] Y. Wang, R. Godin, J.R. Durrant, J.W. Tang, Efficient hole trapping in carbon dot/oxygen-modified carbon nitride heterojunction photocatalysts for enhanced methanol production from CO₂ under neutral conditions, *Angew. Chem. Int. Ed. Engl.* 60 (2021) 20811–20816.
- [32] Z.H. Chen, T. Li, Y. Zhu, X.Y. Liang, Z.Y. Zhao, D. Wang, J.H. Li, Y.W. Gao, C. Hu, Efficient light-free activation of peroxydisulfate by carbon ring conjugated carbon nitride for elimination of organic pollutants, *Chem. Eng. J.* 420 (2021), 129671.
- [33] A. Indra, A. Acharjya, P.W. Menezes, C. Merschjann, D. Hollmann, M. Schwarze, M. Aktas, A. Friedrich, S. Lochbrunner, A. Thomas, M. Driess, Boosting visible-light-driven photocatalytic hydrogen evolution with an integrated nickel phosphide-carbon nitride system, *Angew. Chem. Int. Ed.* 56 (2017) 1653–1657.
- [34] Z.H. Chen, T. Li, Y. Zhu, X.Y. Liang, Z.Y. Zhao, D. Wang, J.H. Li, Y.W. Gao, C. Hu, Efficient light-free activation of peroxydisulfate by carbon ring conjugated carbon nitride for elimination of organic pollutants, *Chem. Eng. J.* 420 (2021), 129671.
- [35] J.Q. Zhang, Y.G. Li, X.L. Zhao, L. Wang, H.J. Chen, S.J. Wang, X.Y. Xu, L. Shi, L. C. Zhang, Y.Z. Zhu, H.Y. Zhang, Y.Z. Liu, G. Nealon, S. Zhang, M.B. Wu, S.B. Wang, H.Q. Sun, Aligning potential differences within carbon nitride based photocatalysis for efficient solar energy harvesting, *Nano Energy* 89 (2021), 106357.
- [36] F. Li, M. Han, Y. Jin, L. Zhang, T. Li, Y. Gao, C. Hu, Internal electric field construction on dual oxygen group-doped carbon nitride for enhanced photodegradation of pollutants under visible light irradiation, *Appl. Catal. B: Environ.* 256 (2019), 117705.
- [37] Q. Qi, Y. Li, H. Liu, B. Li, H. Wang, Y. Lu, W. Gao, Y. Tian, B. Guo, X. Jia, J. Chen, Alkali metal modified carbon nitride enhance photocatalytic performance for highly selective oxidation of benzyl C(sp³)-H bonds, *Appl. Catal. B: Environ.* 319 (2022) 09263373.
- [38] S. Liu, D. Liu, Y. Sun, P. Xiao, H. Lin, J. Chen, X.-L. Wu, X. Duan, S. Wang, Enzyme-mimicking single-atom FeN₄ sites for enhanced photo-Fenton-like reactions, *Appl. Catal. B: Environ.* 310 (2022), 121327.
- [39] J.Q. Zhang, X.H. An, N. Lin, W.T. Wu, L.Z. Wang, Z.T. Li, R.Q. Wang, Y. Wang, J. X. Liu, M.B. Wu, Engineering monomer structure of carbon nitride for the effective and mild photooxidation reaction, *Carbon* 100 (2016) 450–455.
- [40] S.W. Zhang, J.H. Guo, W.J. Zhang, H.H. Gao, J.Z. Huang, G. Chen, X.J. Xu, Dopant and defect doubly modified CeO₂/g-C₃N₄ nanosheets as OD/2D Z-scheme heterojunctions for photocatalytic hydrogen evolution: experimental and density functional theory studies, *ACS Sustain. Chem. Eng.* 9 (2021) 11479–11492.
- [41] L. Ju, Y. Dai, W. Wei, M.M. Li, B.B. Huang, DFT investigation on two-dimensional GeS/WS₂ van der Waals heterostructure for direct Z-scheme photocatalytic overall water splitting, *Appl. Surf. Sci.* 434 (2018) 365–374.
- [42] X.M. Liu, F.T. He, Y.M. Lu, S.L. Wang, C.C. Zhao, S.J. Wang, X.G. Duan, H.Y. Zhang, X.L. Zhao, H.Q. Sun, J.Q. Zhang, S.B. Wang, The double-edged effect of single atom metals on photocatalysis, *Chem. Eng. J.* 453 (2023), 139833.
- [43] I. Grcic, G.L. Puma, Six-flux absorption-scattering models for photocatalysis under wide-spectrum irradiation sources in annular and flat reactors using catalysts with different optical properties, *Appl. Catal. B: Environ.* 211 (2017) 222–234.
- [44] F. Wang, J. Xu, Z.P. Wang, Y. Lou, C.S. Pan, Y.-F. Zhu, Unprecedentedly efficient mineralization performance of photocatalysis-self-Fenton system towards organic pollutants over oxygen-doped porous g-C₃N₄ nanosheets, *Appl. Catal. B: Environ.* 312 (2022), 121438.
- [45] R. Acosta-Herazo, M.A. Mueses, G. Li Puma, F. Machuca-Martinez, Impact of photocatalyst optical properties on the efficiency of solar photocatalytic reactors rationalized by the concepts of initial rate of photon absorption (IRPA) dimensionless boundary layer of photon absorption and apparent optical thickness, *Chem. Eng. J.* 356 (2019) 839–849.
- [46] L. Jing, Y. Xu, J. Liu, M. Zhou, H. Xu, M. Xie, H. Li, J. Xie, Direct Z-scheme red carbon nitride/rod-like lanthanum vanadate composites with enhanced photodegradation of antibiotic contaminants, *Appl. Catal. B: Environ.* 277 (2020), 119245.
- [47] P.J. Mafa, M.E. Malefane, A.O. Idris, D. Liu, J. Gui, B.B. Mamba, A.T. Kuvarega, Multi-elemental doped g-C₃N₄ with enhanced visible light photocatalytic activity: Insight into naproxen degradation, kinetics, effect of electrolytes, and mechanism, *Sep. Purif. Technol.* 282 (2022), 120089.
- [48] Y. Chen, L. Liu, J. Su, J. Liang, B. Wu, J. Zuo, Y. Zuo, Role of humic substances in the photodegradation of naproxen under simulated sunlight, *Chemosphere* 187 (2017) 261–267.
- [49] L. Chen, J. Duan, P. Du, W. Sun, B. Lai, W. Liu, Accurate identification of radicals by in-situ electron paramagnetic resonance in ultraviolet-based homogenous advanced oxidation processes, *Water Res.* 221 (2022), 118747.
- [50] L. Chen, H. Ji, J. Qi, T. Huang, C.-C. Wang, W. Liu, Degradation of acetaminophen by activated peroxydisulfate using Co(OH)₂ hollow microsphere supported titanate nanotubes: Insights into sulfate radical production pathway through CoOH⁺ activation, *Chem. Eng. J.* 406 (2021).
- [51] N. Jallouli, K. Elghijji, O. Hentati, A.R. Ribeiro, A.M. Silva, M. Ksibi, UV and solar photo-degradation of naproxen: TiO₂ catalyst effect, reaction kinetics, products identification and toxicity assessment, *J. Hazard. Mater.* 304 (2016) 329–336.
- [52] Y.F. Wang, B.H. Jing, F.L. Wang, S.C. Wang, X. Liu, Z.M. Ao, C.H. Li, Mechanism Insight into enhanced photodegradation of pharmaceuticals and personal care

- products in natural water matrix over crystalline graphitic carbon nitrides, *Water Res* 180 (2020) 0043–1354.
- [53] B. Peng, L.Y. Wu, Q.Z. Li, Q.W. Wang, K.Z. Li, Z.Y. Zhou, Photodegradation of naproxen using CuZnAl-layered double hydroxides as photocatalysts, *Crystengcomm* 24 (2022) 5080–5089.
- [54] F.L. Wang, Y.F. Wang, Y.P. Feng, Y.Q. Zeng, Z.J. Xie, Q.X. Zhang, Y.H. Su, P. Chen, Y. Liu, K. Yao, W.Y. Lv, G.G. Liu, Novel ternary photocatalyst of single atom-dispersed silver and carbon quantum dots co-loaded with ultrathin g-C₃N₄ for broad spectrum photocatalytic degradation of naproxen, *Appl. Catal. B: Environ.* 221 (2018) 510–520.
- [55] H. Wang, S. Jiang, S. Chen, D. Li, X. Zhang, W. Shao, X. Sun, J. Xie, Z. Zhao, Q. Zhang, Y. Tian, Y. Xie, Enhanced singlet oxygen generation in oxidized graphitic carbon nitride for organic synthesis, *Adv. Mater.* 28 (2016) 6940–6945.